

Lawrence Berkeley National Laboratory

LBL Publications

Title

Collaborative development of diffraction-limited beamline optical systems at US DOE light sources

Permalink

<https://escholarship.org/uc/item/56r942xj>

ISBN

9781510629110

Authors

Goldberg, Kenneth A
Wojdyla, Antoine
Bryant, Diane
et al.

Publication Date

2019-09-09

DOI

10.1117/12.2530817

Peer reviewed

Collaborative development of diffraction-limited beamline optical systems at US DOE light sources

Kenneth A. Goldberg^{*a}, Antoine Wojdyla^a, Diane Bryant^a, Weilun Chao^a, Daniele Cocco^{a,b}, Corey Hardin^b, Daniel Morton^b, May Ling Ng^b, Lance Lee^b, Lahsen Assoufid^c, Walan Grizolli^c, Xianbo Shi^c, Steve P. Kearney^c, Michael Wojcik^c, Yuri Shvyd'ko^c, Deming Shu^c, Mourad Idir^d, and Lei Huang^d

^aLawrence Berkeley National Laboratory, Berkeley, CA USA 94720;

^bSLAC National Accelerator Laboratory, 2575 Sand Hill Rd. Menlo Park, CA, 94025;

^cArgonne National Laboratory, 970 S. Cass Avenue, Argonne, IL USA 60439;

^dBrookhaven National Laboratory, Upton, NY USA 11973

ABSTRACT

An ongoing collaboration among four US Department of Energy (DOE) National Laboratories has demonstrated key technology prototypes and software modeling tools required for new high-coherent flux beamline optical systems. New free electron laser (FEL) and diffraction-limited storage ring (DLSR) light sources demand wavefront preservation from source to sample to achieve and maintain optimal performance. Fine wavefront control was achieved using a novel, room-temperature cooled mirror system called REAL (resistive element adjustable length) that combines cooling with applied, spatially variable auxiliary heating. Single-grating shearing interferometry (also called Talbot interferometry) and Hartmann wavefront sensors were developed and used for optical characterization and alignment on several beamlines, across a range of photon energies. Demonstrations of non-invasive hard x-ray wavefront sensing were performed using a thin diamond single-crystal as a beamsplitter.

1. INTRODUCTION

New facilities and planned major lightsource upgrades at four U.S. Department of Energy (DOE) National Laboratories are driving an intense effort to develop beamline optical systems that are matched to the new source properties of free electron lasers (FEL) and diffraction limited storage rings (DLSR). With a focus on delivering high coherent flux to demanding experimental applications in scattering, dynamics, and nanoscale probes, the tolerances on optical components have never been more stringent. With minute surface and alignment errors affecting the wavefront downstream, new beamlines must be treated as interdependent optical systems, where adaptive corrections coupled to high accuracy feedback are ultimately required to achieve and maintain the wavefront properties in routine operations.

Shared goals and common interests spurred an active, ongoing collaboration among beamline scientists at Argonne National Laboratory (ANL), Brookhaven National Laboratory (BNL), Lawrence Berkeley National Laboratory (LBNL) and SLAC National Accelerator Laboratory (SLAC). Sponsored by the DOE's Office of Science, Basic Energy Science (BES) Division, our two-year project demonstrated key soft x-ray (SXR) and hard x-ray (HXR) instrumentation prototypes.

Within the project, our teams demonstrated fine wavefront control using a novel, room-temperature, cooled mirror system called REAL (resistive element adjustable length) that combines cooling with applied auxiliary heating, tailored to the spatial distribution of the incident thermal load [1, 2]. Where applicable, this technique is capable of achieving sub-nanometer surface figure error, and in theory, it can do so even at extreme power density.

Experimental applications on high performance beamlines where high coherent flux is a dominant concern will also need to measure the x-ray wavefront in real time, including during sample measurements, to provide feedback for active optical elements. Such sensors must ideally not unduly perturb the probe beam while they provide information for beamline alignment and optimization. We refer to this as "non-invasive" testing. The development of both invasive and non-invasive sensor designs was part of this program. Single-grating shearing (also called Talbot) interferometry and Hartmann wavefront sensing were developed and also used for optical characterization and fine alignment on several beamlines at a

range of photon energies [3], and as feedback for mirror wavefront measurements [4, 5, 6]. Demonstrations of non-invasive HXR wavefront sensing were performed using a diamond single crystal as a beam splitter [7].

Software tools are essential in the design and modeling of modern beamlines. This includes the continued advancement of ray-tracing tools, in support of coherent optical systems, and wave-optical tools for modeling and analyzing beamlines and including wavefront sensors, including the analysis of wavefront measurement data.

This paper describes the development and demonstration of the key technologies within the project.

2. DEVELOPMENT AND IMPLEMENTATION OF THE REAL COOLING SYSTEM

In the first year of the project, we demonstrated that the REAL cooling system works according to the project design.

2.1 Description of the REAL mirror and assembly

REAL is an active mirror cooling system for high-power beamline mirrors, developed to reduce the effect of local, beam-induced thermal deformation on the reflected light's wavefront. It combines cooling with applied auxiliary heating that is actively tailored for the spatial distribution of the incident thermal load. As the beam footprint and power vary with photon energy on beamlines powered by insertion devices, REAL's array of heaters delivers spatially distributed power to the mirror in a complementary manner. In this way, the mirror surface deformation can be minimized.

As implemented, REAL uses a trough-cooled setup, shown in Fig. 1, with several resistive heaters added and bonded to the side of each blade, at a safe, non-contact distance from the gallium-indium eutectic. The electric heaters are wired through electric feedthroughs for remote control. Platinum resistance temperature detectors (RTD) and/or thermocouples are used to monitor system temperatures for feedback.

Active mirror-shaping tests performed in the metrology laboratory of SLAC showed that the mirror could compensate a thermal bump deformation induced by infrared laser heating. The compensation restored the original mirror flatness (i.e. profile). The system is shown in Figs. 1 and 2.

Since 2015 several technical improvements were made in preparation for beamline tests with synchrotron radiation, including making the heating and cooling system UHV compatible. The linearity of the power delivered to the mirror was improved, based on 100 Hz, pulse-width modulation control. A shape prediction algorithm able to correct the mirror bump was developed and tested.

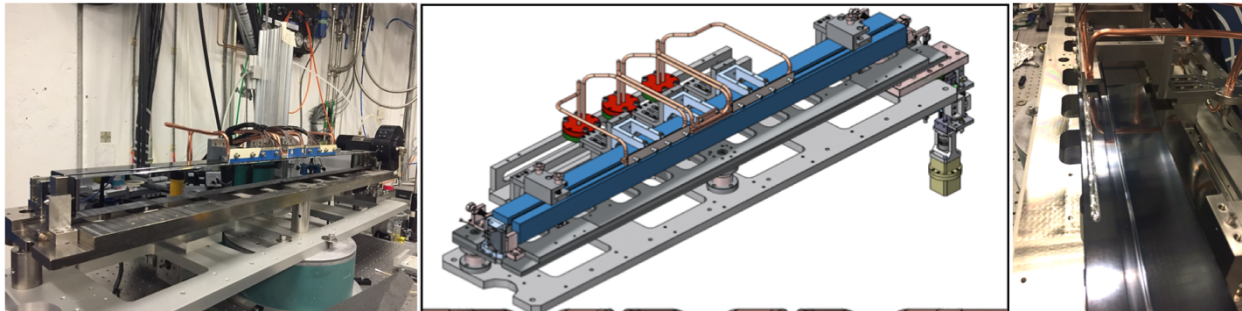


Figure 1. The 1-m-long mirror used for most of the tests performed during the project. CENTER: A CAD model of the mirror, with the cooling pads and the holder. LEFT: The reflecting surface of the mirror is shown. The cooling circuits are above it, and the blue and white heaters are visible. RIGHT: A photo of the top of the mirror, showing the GaIn eutectic partially filling the trough.

2.2 Testing two different thermal conduction modes

To assess different types of thermal contact, the REAL cooling scheme was tested on two classes of mirrors. First, a one-meter-long mirror, cooled through a series of Cu pads immersed in a trough filled with gallium-indium (GaIn) eutectic (see Fig. 1). Here, the cooling pads are physically separated from the mirror and the thermal contact happens through the eutectic. In this way, any expansion due to the heaters, or vibrations induced by the water flow, is not transmitted directly to the mirror. We found that this was the most convenient solution.

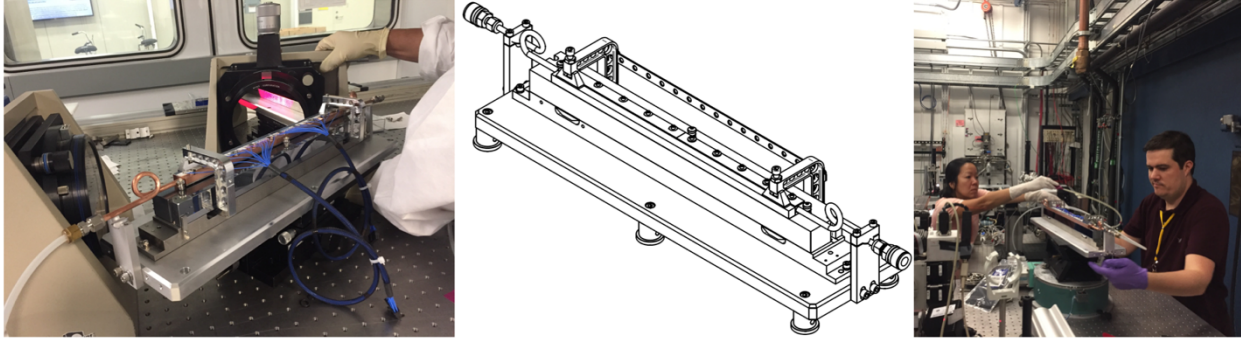


Figure 2. The mirror and the holder for testing the potential use of REAL with direct side cooling via indium foil. CENTER: The cad model of the mirror with the cooling circuit and the clamps for holding the cooling pads in contact with the mirror. LEFT: Photo of the mirror in the APS metrology laboratory in preparation for the tests. RIGHT: Installation of the mirror on the 7-ID beamline at the APS in preparation for the test with X-rays.

The second cooling contact method we tested used indium foils pressed between the cooling units and the mirror; a method widely used in the SXR community. An old LCLS mirror was used to test this concept in conjunction with the REAL cooling (see Fig. 2). Using indium foils in this way has the advantage that the mirror can be characterized in a metrology laboratory and safely transported to its beamline. While this method is widely used within the x-ray optics community, the era of diffraction limited storage rings pushes us into a new domain of precision mechanics and mirror assemblies. The limitations imposed by potential distortion from thermal cycling is a significant concern for this approach.

Test showed that in practice, the REAL system with direct contact indium foils is difficult to implement. When the pads are heated, the density of the indium foil changes and reduces the force applied by the clamps. Then, when the mirror is cooled, the clamps tend to compress the mirror and deform the optical surface. At the nanometer scales relevant for wavefront preservation, these thermal deformations become significant. Furthermore, the copper pads spread the heat effectively across their areas, broadening the temperature profile and reducing local control of the heating. In contrast, the GaIn cooling demonstrates a more localized response.

An improved setup for the 1-m mirror prototype was implemented and tested successfully at the APS 7-ID beamline in October 2018. The results are described in the subsequent section.

3. EXPERIMENTAL TESTS OF THE REAL MIRROR AT THE APS BEAMLINE 7-ID

The physical shape responses of the mirror surface to heating from the isolated individual actuator elements are called the *influence functions*, and they are central to the process of adaptive correction. During the second round of REAL mirror tests, conducted at APS beamline 7-ID in October 2018, we measured the influence functions, tested the performance of two interferometers, and demonstrated the compensation of thermal distortion errors in a predictable way.

3.1 Description of the mirror and wavefront sensor configurations

The 1-m-long mirror tested at APS beamline 7-ID features a cradle with a bender mechanism and water-cooled heating blades (visible in Fig. 3) submersed in eutectic liquid GaIn for heat conduction, as described above. The heating blades were individually controlled with analog commands as described in section 2.2. The mirror has an inherent 2-nm-rms shape error.

Two x-ray wavefront sensors were used to test the mirror: a shearing interferometer (also called a “Talbot wavefront sensor”), [4, 5, 8, 9] and a Hartmann wavefront sensor [10–12].

The Talbot wavefront sensor is based on a transmission phase grating (4.8- μm period gold checkerboard with $\pi/2$ phase shift (Fig. 4, left), a YAG scintillator with interchangeable microscope objectives of 10 \times and 5 \times , and a visible-light CMOS camera. The Hartmann sensor (Fig. 4, right) has a hole-grid with 20- μm pitch, and is also based on the visible-light reimaging of a scintillator-based detection. The Talbot wavefront sensor was used to measure changes relative to the reference measurement. The data was analyzed using a custom software (*WAVEPY*) developed at the APS as part of the project [see Section 7.2]. The Hartmann sensor provided calibrated wavefront measurements using data acquisition based

on commercial software for real-time operation and advanced analysis (developed by *Imagine Optic SA*, France). The feedback to the mirror's heater, in this case, has been realized through a custom software developed at SLAC.

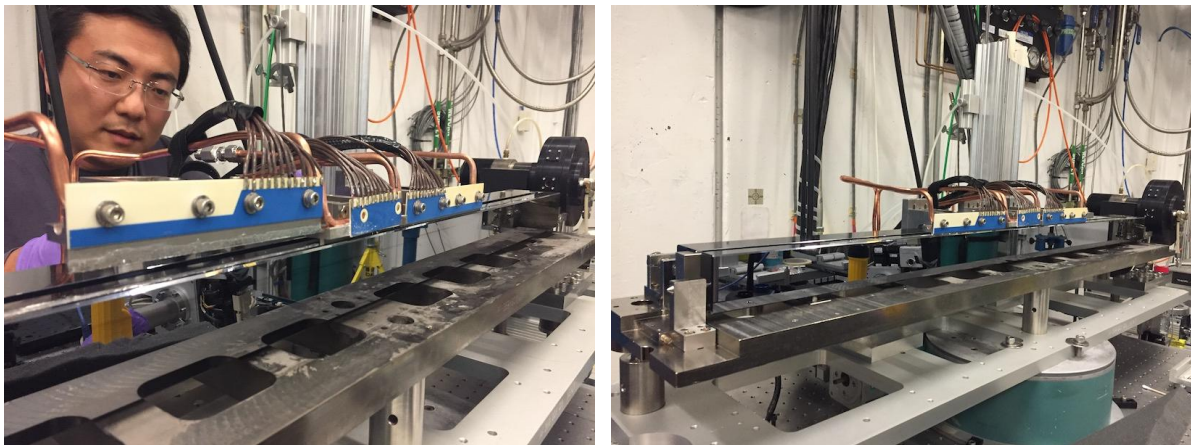


Figure 3. (LEFT) 1-m mirror with heating blades during installation. (RIGHT) Mirror assembled, at the beamline.

3.2 Measuring the thermal response of the mirror under varying power loads

To vary the x-ray-induced heat load on the mirror, the undulator gap was reduced from 50 mm (corresponding to 14 keV photon energy and low power) to 28 mm (corresponding to 12.5 keV and higher power).

The incidence angle of the beam on the REAL mirror was set to 4 mrad to intentionally absorb about 99% of the incident power. In this way, we reduced the power delivered to the wavefront sensors, preventing damage and saturation, while providing high thermal load for testing.

The thermally-induced deformation of the mirror surface was observed in the wavefront measurements as the undulator gap was changed (see Fig. 5).

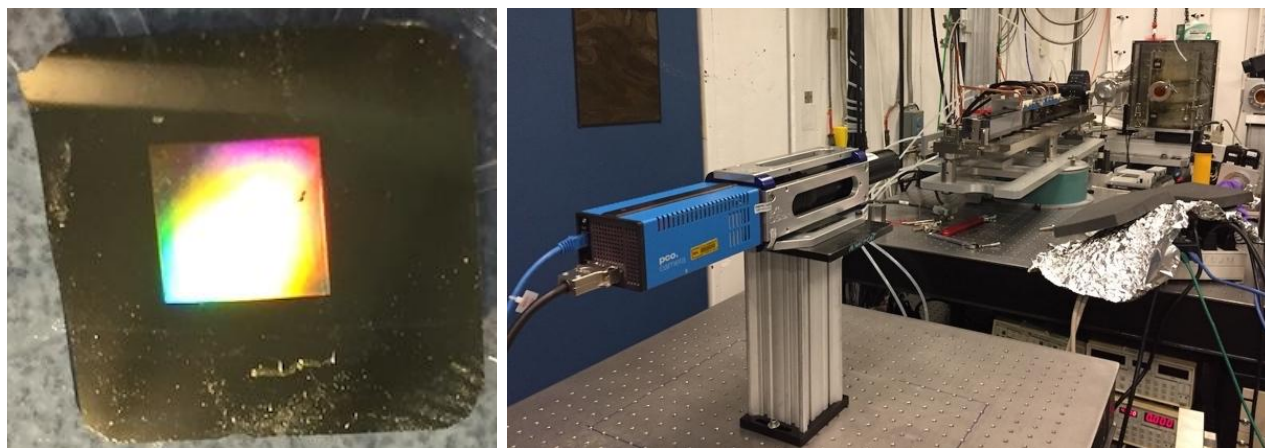


Figure 4. (LEFT) Shearing grating of the Talbot wavefront sensor. (RIGHT) Hartmann sensor.

The influence functions (also called *characteristic functions*) were measured at-wavelength using a low-power x-ray beam. Each heater was activated separately and the wavefront *change* was observed, simply as the difference between two measurements. This characterization was performed using both Talbot and Hartmann wavefront sensors in two separate experiment runs. The measurements were self-consistent within our measurement uncertainty, even though the tests were performed several days apart, and the temperature in the hutch changed by several degrees.

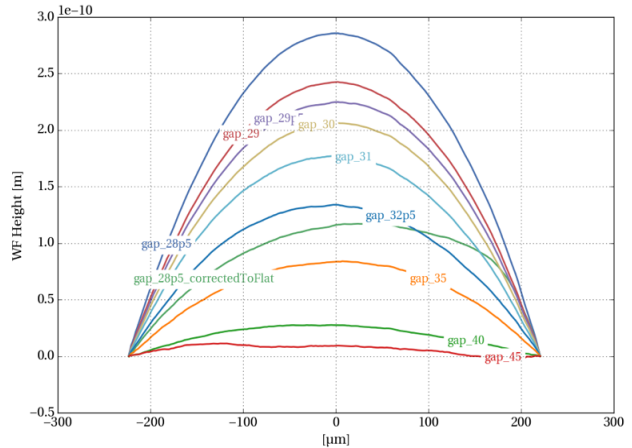
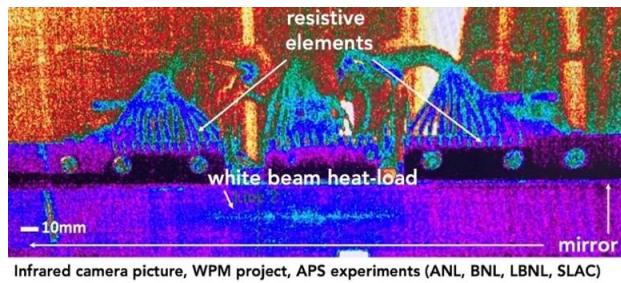


Figure 5. (LEFT) Beam footprint on the mirror recorded using an IR camera. (RIGHT) Measured thermal deformations resulting from different input conditions, varying the undulator gap (smaller gaps yield higher power). Note that at 4 mrad incidence angle, the optical path length change induced by a surface height error, h , is $h/125$.

3.3 Compensating measured wavefront errors

From the set of measured influence functions, we can calculate the input power values for each electrode to correct arbitrary thermally-induced wavefront distortions. In our tests, corrections were successfully applied in two or three converging steps. We found that following the first step, only small adjustments were required to reach the target shape.

One example from the Hartmann sensor is shown in Fig. 6. The ability to converge quickly to the optimal shape is a demonstration of the linearity of the system’s response. In principle, this property could allow open loop operation on a beamline: e.g., performing actuation to compensate an expected thermal bump, knowing the power and profile of the incoming beam in advance.

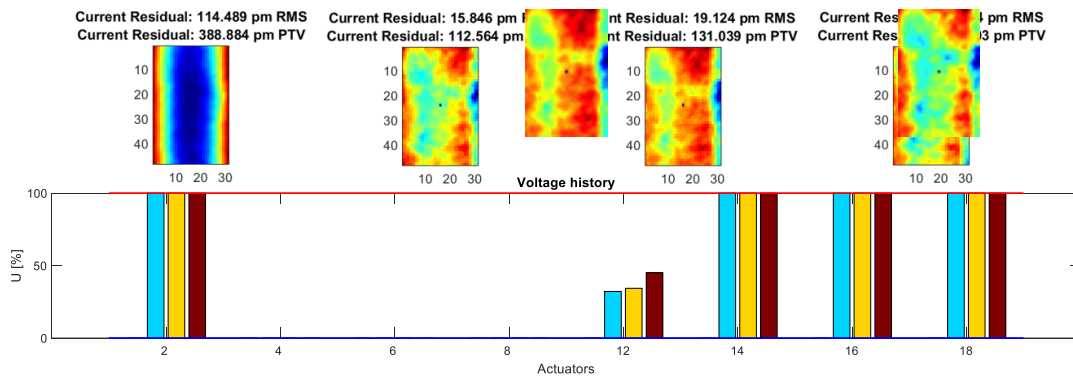


Figure 6. Compensating a measured wavefront error. (ABOVE) A sequence of measured wavefront errors, reduced over three steps. (BELOW) Input power percentage given to the various heater channels: 1st iteration, blue bars; 2nd iteration, yellow bars; 3rd iteration, maroon bars.

An example using the Talbot wavefront sensor is shown in Fig. 7. Here, two different x-ray beam footprints were delivered to the mirror by opening an upstream beam-defining aperture. The wavefront error caused by the thermal bump can be corrected to a level of approximately $\lambda/15$ rms. This corresponds to a height error of 0.8-nm rms on the mirror surface, consistent with the requirements for diffraction-limited optics.

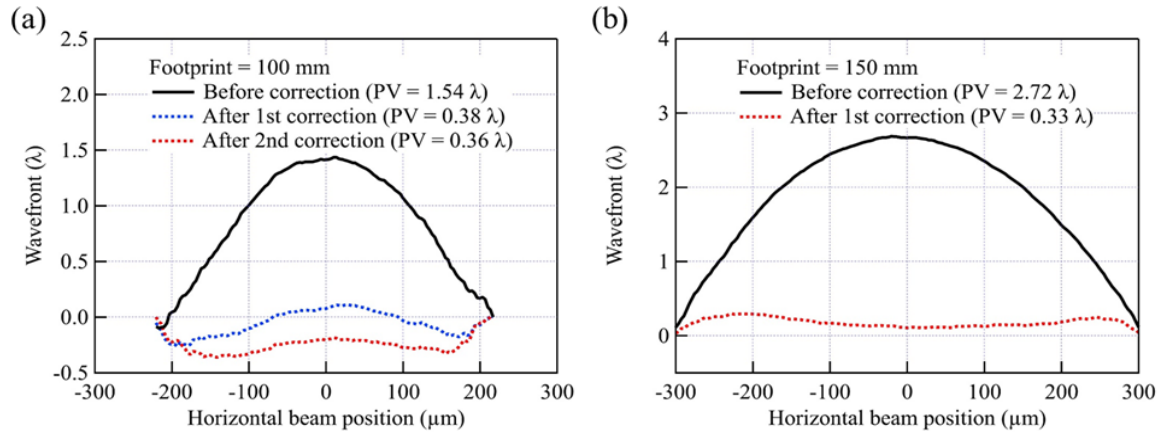


Figure 7. Wavefront correction with two thermal footprints: (a) 100-mm length, and (b) 150-mm length.

3.4 Characterizing the temporal response

The temporal response of the individual heater elements is an important consideration for the operation of the REAL mirror. We found that the heaters take about 40 seconds to reach their peak temperature, and achieved a steady state temperature in about 5 minutes, as shown in Fig. 8, left. This shows the approximate timescale over which the REAL mirror can react to changing beam conditions. It is also interesting to note the relationship between the heating element temperature and the deformation induced on the mirror is nearly linear (Fig. 8, right).

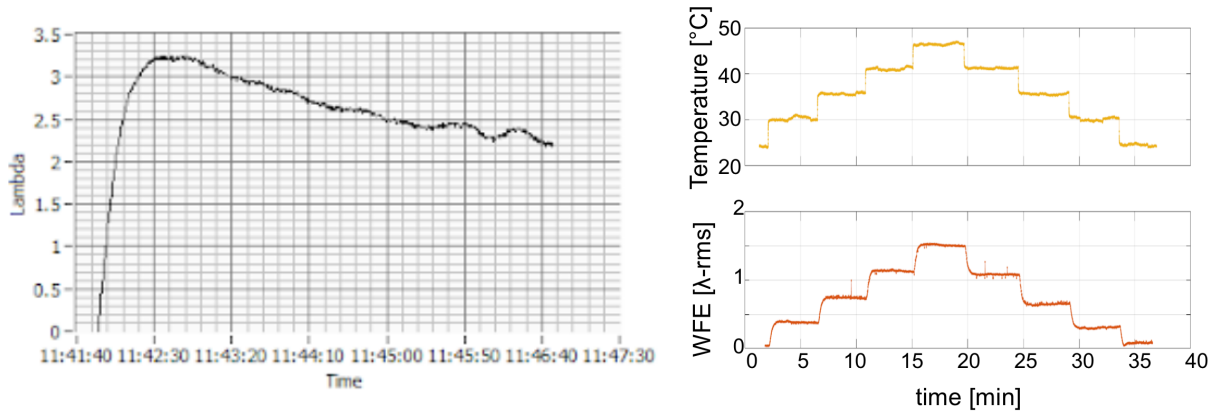


Figure 8. (LEFT) Time dependence of the mirror deformation measured by the wavefront sensor when the power is applied to a heater. It takes about 40 seconds to reach the peak value and few minutes to reach equilibrium. (RIGHT, top) Step changes in the heating element power, shown in terms of resultant temperature. (RIGHT, bottom) Observed mirror wavefront error (WFE) response measured by the Hartmann sensor.

3.5 Ultra-high vacuum (UHV) implementation of the REAL mirror

The tests performed in the SLAC metrology laboratory, and at APS beamline 7-ID, were done in air. Ultimately, operation at soft x-ray wavelengths requires mirrors to operate under strict UHV conditions to avoid or minimize carbon contamination over time. It is therefore essential to ensure that all of the mirror's components are compatible with UHV operation.

To ensure UHV compatibility of the heaters, a review of materials was performed with the vendor. A process was developed to create the heaters from only three materials: aluminum oxide for the substrate, silver for the wire traces, and glass for the insulating layer. The heaters are produced by a thick-film printing technique, with the silver and glass utilizing a binder. The heater is then fired at high temperature to remove the binder and leave only a UHV-compatible system. A CAD model of the heater for the distribution mirrors of LCLS II and a photo of the heaters are shown in Fig. 9.

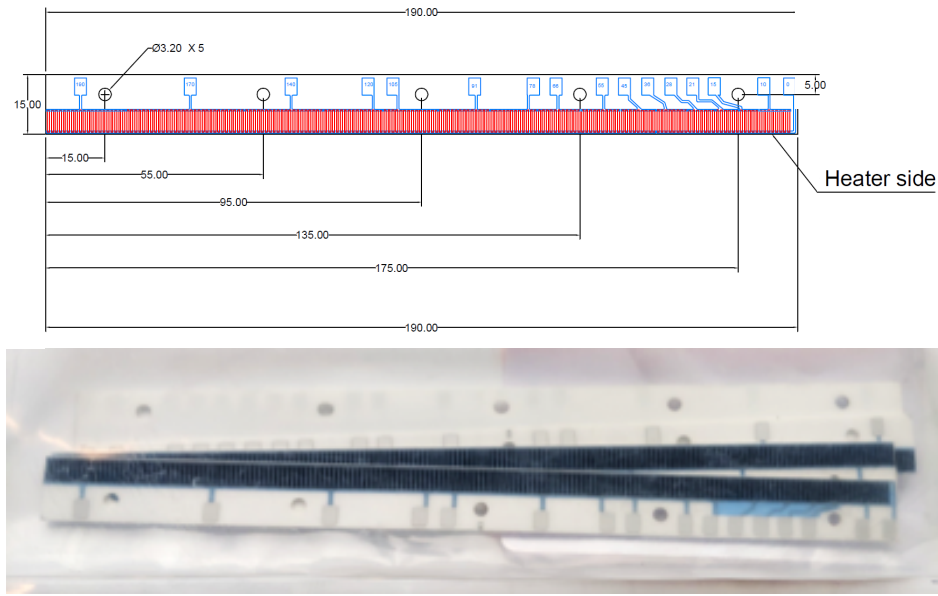


Figure 9. (ABOVE) CAD model of the heater showing the resistors (red) and the contacts (light blue). The holes on the aluminum oxide substrates (black) are used to fix the heaters to the cooling rails. (BELOW) Photograph of the heaters, in clear bags, after RGA testing.

To verify the UHV compatibility of the final product, residual gas analyzer (RGA) testing was performed on four heaters using a standard SLAC bakeout/verification procedure. The heaters were first baked to 250°C. Once the pressure stabilized in UHV conditions ($\sim 1 \times 10^{-8}$ Torr), the temperature was reduced to 150°C and an RGA scan was performed. Finally, an RGA scan performed at room temperature showed partial pressures of the various, relevant gas species below 1×10^{-10} Torr, suitable for UHV beamline operation.

4. HARTMANN WAVEFRONT SENSOR DEVELOPMENT AND TESTING

4.1 Hard x-ray Hartmann wavefront sensor technique at BNL and ANL

The Hartmann wavefront sensor (HWS) configuration is commonly used for optics testing [10–12] and especially in conjunction with adaptive optics in the visible light regime. The HWS we developed is based on the design first implemented at synchrotrons in 2002 [11]. The wavefront is analyzed by dividing the incoming beam into small areas/spots and using projected light to measure the wavefront's two-dimensional gradient at each position. In practice, the beam illuminates a grid of regularly spaced holes, and individual, non-overlapping spots are projected some distance onto the detector (as shown in Fig. 10.). Aberrations affect the local slope of the wavefront incident on the grid and shift the observed positions of the *beamlets*. The local wavefront gradients are inferred from the direction and magnitude of the beam position shifts, and the distance from the grid to the detector. This discrete sampling of the wavefront gradient is used to mathematically reconstruct an approximation to the original wavefront.

The angular sensitivity of the technique is limited by the precision with which the spot positions can be measured and the distance from the hole grid to the detector plane (whether a YAG scintillator or a direct-detection x-ray camera.) The grid must be relatively opaque because unwanted light leaking through the absorptive regions of the screen can degrade the measurement. In practice, the sensitivity to low-spatial-frequency aberrations (defocus, astigmatism, coma, etc.) is higher than the precision of a single beamlet because many individual measurements are combined.

The accuracy of the HWS technique relies on calibration. In many cases, an ideal reference beam with a known radius is generated using a spatial-filter pinhole. Spot displacement measurements are then made relative to this established calibration, and in this way, measurements accommodate imperfections in the hole grid fabrication.

Once the local *x*- and *y*-direction gradient values have been determined from the spot displacements, the wavefront can be reconstructed. Several wavefront reconstruction methods have been used during the project, including modal methods

(based on fitting polynomial shapes) [13, 14] and zonal methods (which rely on self-consistent local comparisons) [15–17]. For the REAL mirror tests at APS, we adopted the spline-based least-squares integration (SLI) method to reconstruct the wavefront shapes. In the SLI method, slope data are fit with cubic splines to represent wavefront differences between points. We estimate the wavefront distributions with the linear least-squares method, which can best explain the measured slope in the spline-expressed relations. Once the wavefront slopes are obtained, then the wavefront itself can be reconstructed using various numerical integration methods. The method of Ref. 13 was used in this case.

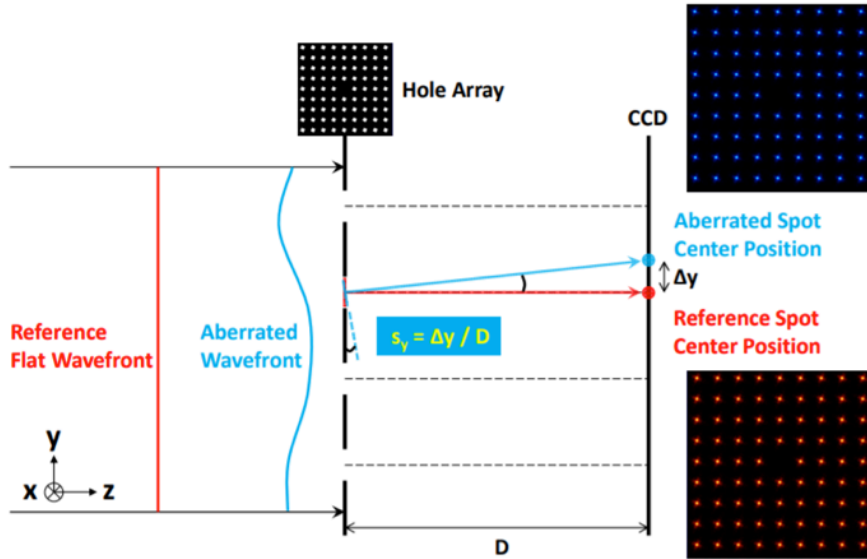


Figure 10. Principle of the Hartmann wavefront sensor (HWS) shown in one dimension. The displacement of the spots, Δy , with respect to the calibrated positions is proportional to the mean local wavefront tilt across the hole and the distance between the grid and the detector plane.

4.2 Hartmann wavefront sensor design considerations

The basic rules for dimensioning the Hartmann mask is to have holes small enough to create diffraction on the CCD plane, and a hole pitch large enough to avoid overlapping (“crosstalk”). While increasing the grid-to-detector distance could provide greater sensitivity, wavelength-dependent diffraction increases the width of the spots on the detector plane causing overlapping at a certain distance. The design faces a tradeoff between hole separation and the spatial sampling (i.e. the number of points) across the wavefront. Decreasing the hole size reduces the light flux and strongly affects the power density by increasing the diffraction angle. However, when there are sufficient photons, spot positions are more easily measured when the diffracted beams span a larger number of pixels. The optimal balance between these effects has been studied, and is described below.

4.3 Hartmann wavefront sensor expected performance

Both of the commercial Hartmann wavefront sensors (the SXR and the HXR versions) were optimized and manufactured in close collaboration with *Imagine Optic SA*. The HXR wavefront sensor has been used for the tests performed at APS (HXR), that led to the results shown below. Images of the system and a plot of the expected accuracy versus photon energy are shown in Fig. 11.

Since the sensor was not yet calibrated for accuracy, its reproducibility was tested by measuring the difference between consecutively measured wavefronts. The resulting residual wavefronts are displayed in Fig. 12. One-hundred measurements were made, then tilt, piston, and the average wavefront is subtracted from each. At a wavelength of 0.1 nm, the reproducibility derived from these measurements is 3.43 pm, $\sim\lambda/29$ rms. We believe that the piston and tilt terms arise from vibration only. If, in addition, the power term (corresponding to the distance from the mirror to the sensor) is subtracted as well, the rms discrepancy drops to 1.77 pm, $\sim\lambda/56$.



Figure 11. LEFT, rendering of the optimized HXR wavefront sensor at *Imagine Optic SA*. CENTER, The WFS installed at the APS 7-ID beamline. RIGHT, Calculated accuracy of the wavefront sensor, compared with a $\lambda/100$ value.

Better reproducibility and noise reduction can be attained after averaging, with the expected signal-to-noise ratio following $1/\sqrt{N}$, with N being the number of measurements, however the measured repeatability is already acceptable for most beamline optimization procedures.

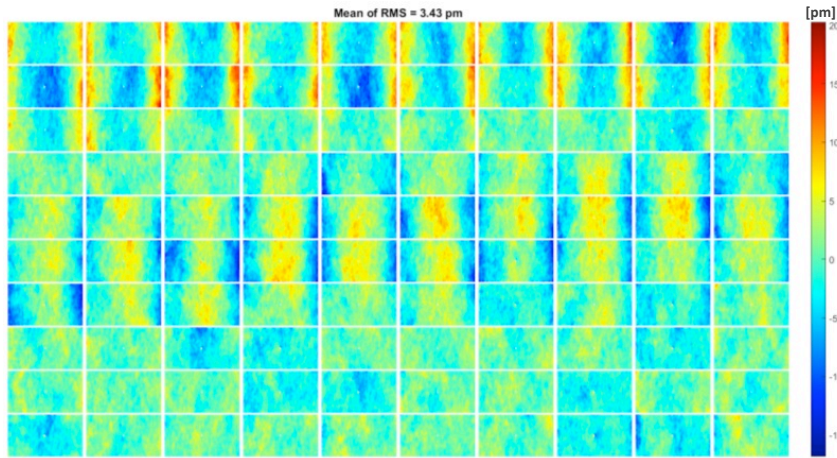


Figure 12. Residual wavefront difference after subtraction of the average measured wavefront. The measurements were made with a wavelength of 0.1 nm; the reproducibility is calculated to be $\sim\lambda/29$ (3.43 pm) rms.

4.4 Application of Hartmann testing to SXR beamline alignment at the ALS

The ALS's COSMIC is a recently commissioned SXR insertion device beamline featuring branches for x-ray diffractive imaging (ptychography) and scattering (XPCS), shown in Fig. 13. Modeling showed a strong dependence of the astigmatism with the angle of the toroidal M112 mirror, providing an opportunity for a wavefront sensor to be used to optimize the beam focusing and gain comparison with modeling.

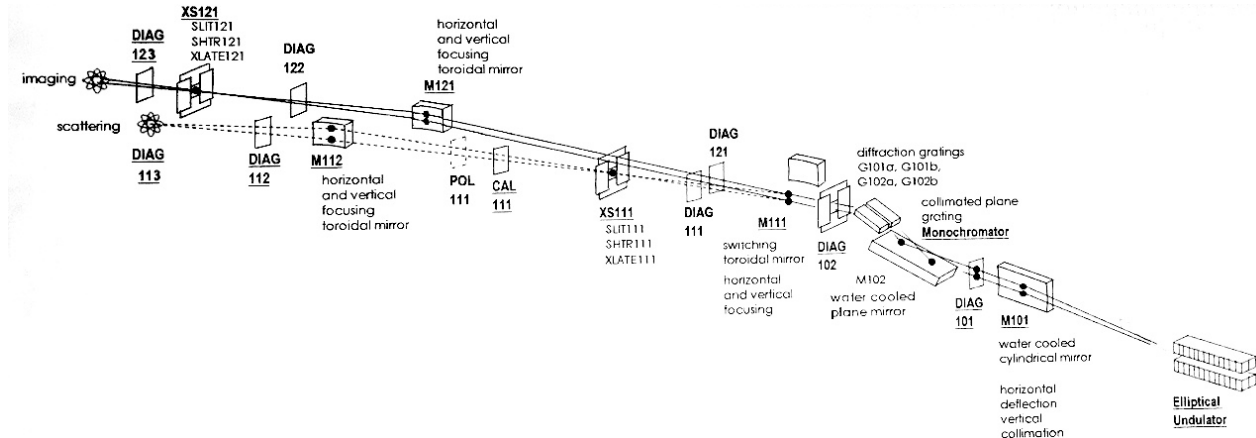


Figure 13. Schematic Layout of the ALS's COSMIC beamline, with the beam propagating from right to left. The alignment of one branch was optimized using Hartmann wavefront sensor feedback.

The converging wavefront produced by the beamline optics was measured using an *Imagine Optic* HASO SXR (Hartmann) wavefront sensor, which uses a direct-detection x-ray CCD camera. The small beam subtended 12×15 spots on the Hartmann grid—sufficient for measurement of the low-spatial-frequency aberrations.

Figure 14 shows a single measured Hartmann-gram, along with three wavefronts recorded during the iterative alignment procedure. Knowing that the beam is focusing toward the exit slit plane, the large focus term is removed from the measured wavefront shape, revealing the astigmatism. The residual shape contains the astigmatism we wish to correct, and a smaller coma as well. To perform the alignment and characterization, we assessed the wavefront dependence on the primary available degree of freedom, the mirror tilt. In our tests the mirror was tilted in small angular increments, and the wavefront was recorded at each position.

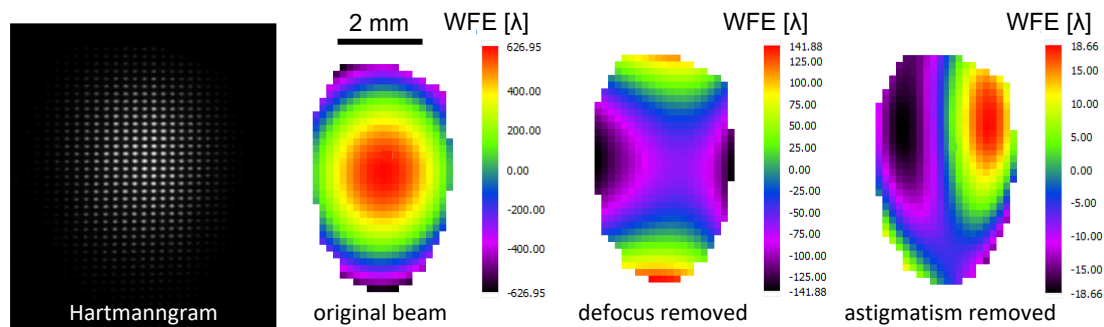


Figure 14. Hartman tests were used to iteratively align a toroidal mirror on the ALS’s COSMIC beamline and verify modeling. (a) Hartmann-gram test image. (b) Original wavefront with defocus. (c) Astigmatism-dominated residual wavefront, with focus removed. With the beamline aligned to eliminate the astigmatism, (d) the final wavefront is dominated by residual coma. Measurements were made with 2.5-nm-wavelength light.

Following alignment, the residual coma aberration from the toroidal mirror is expected and apparent. Comparison of the rate of change of astigmatism with mirror angle, made between the measured data and the optical modeling, converged to within the measurement uncertainty level. This test was recently reported by Wojdyla [18].

5. NON-INVASIVE HARD X-RAY WAVEFRONT SENSORS

The non-invasive wavefront sensor studied during this program is based on single-grating shearing (Talbot) interferometry technique combined with a thin, diamond single-crystal beam splitter [7]. The initial tests of the non-invasive wavefront sensing were performed at the APS beamline 1-BM-C experimental station in October 2017 and 1-BM-B station in March 2018 using two different bimorph mirrors and experimental setups.

5.1 A diamond beamsplitter for non-invasive wavefront sensor applications

A dedicated prototype instrument, namely “a compact non-invasive wavefront sensor for hard x-rays” was designed in 2017, assembled and tested at APS 1-BM and 7-ID beamlines in 2018. The crystal assembly holds a single-crystal beam splitter with a high-precision rotation stage for Bragg-angle scan. The crystal holder is designed with a U-shaped cut-out to allow the transmitted beam pass through. We tested several thin, diamond single-crystals and selected one diamond (111) crystal of 100- μm thickness to be used for all tests and measurements.

The grating and detector assemblies are placed on a two-theta rotation arm aligned to intercept the beam diffracted from the crystal at twice the Bragg angle. The gratings used for hard x-rays are 2D checkerboard phase gratings with π or $\pi/2$ phase shift and different periods, typically 4.8 μm , for different x-ray energies [19, 20]. The assembly contains a visible-light camera (GS3-U3-120S6M-C, *FLIR Integrated Imaging Solutions Inc.*), a 45° reflecting mirror, a $10\times$ or $5\times$ objective lens, and a scintillator (see Fig. 15.) The interferometer was commissioned in February 2018, including the mechanical, electronic, control, and acquisition systems.

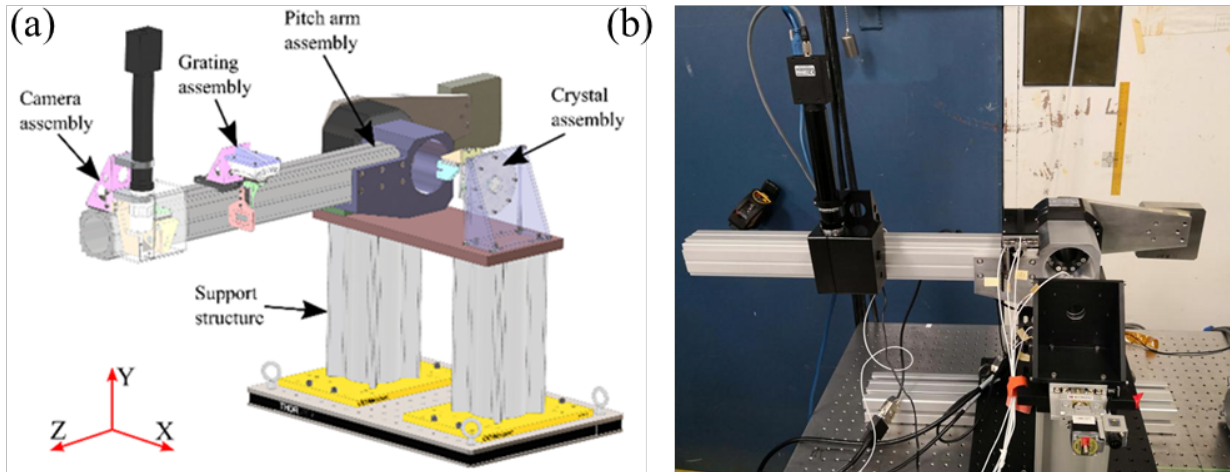


Figure 15. (a) model, and (b) photo of the non-invasive interferometer built at Argonne.

5.2 Deformable test mirror

The sensor was first tested using an ultra-high precision, deformable mirror assembly acquired from JTEC [21]. The assembly consists of a flat Si mirror with a Pt coating, an optical aperture of $150 \times 8 \text{ mm}^2$, a kinematic mounting holder, a multi-channel high-voltage power supply, and an electronic control unit. The mirror surface is polished to a figure error of 2.18-nm peak-to-valley (PV), 0.17-nm rms roughness.

The deforming system consists of a series of piezoelectric actuators (lead zirconate titanate, PZT) controlled by the high-voltage power supply. The mirror has 18 individual segmented actuators (channels 1 through 18) equally spaced over the surface, and one additional actuator at the bottom (channel 19), extending the full length of the mirror. The full-length actuator is used as the main bender, defining the overall curvature of the mirror, while the individual channels can be used to correct local imperfections. The actuators are controlled by a high voltage power supply with 19 outputs with a range of $\pm 500 \text{ V}$.

5.3 Mirror and non-invasive wavefront sensor testing

Several beamtimes (July, August, and November 2018) at 1-BM-B beamline were dedicated to testing the non-invasive wavefront sensor, with the help of the deformable mirror. We demonstrated that the wavefront of the diffracted beam can be used to monitor and correct the direct beam non-invasively. The November 2018 results are presented here.

The deformable mirror was pre-set to a near flat condition; the direct beam (after the mirror reflection but with the beam-splitter crystal removed) and the diffracted beam (after the mirror reflection and crystal diffraction) were measured as a reference condition. The channel 19 electrode voltage was then increased by 20 V to serve as the mirror-shape or beam-wavefront perturbation.

The wavefront of the diffracted beam was then corrected based on the measured influence functions from channels 1 through 18, and the original profile was nearly restored. Figure 16 shows that after only two iterations, the wavefront error of the diffracted beam was corrected to $0.08 \lambda \text{ PV}$ ($0.02 \lambda \text{ rms}$) from its reference condition, limited only by the precision of the measurement. After the correction, the measured direct beam wavefront had an error of $0.40 \lambda \text{ PV}$ ($0.11 \lambda \text{ rms}$) from its reference condition. In this way, the two measurements (direct and diffracted beams) provide a calibration that allows the measurement of the diffracted beam to be used to correct the direct beam.

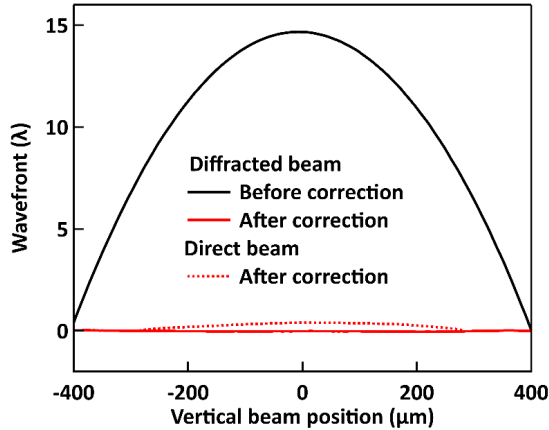


Figure 16. Measured wavefront error from the reference condition while correcting the diffracted beam. The diffracted beam's wavefront error (solid lines) was reduced to 0.08λ PV (0.02λ rms), limited by the precision of the measurement. The direct beam's wavefront error after correction (dashed line) was 0.40λ PV (0.11λ rms).

6. SOFT X-RAY WAVEFRONT SENSOR DEVELOPMENT

A major portion of the work conducted by LBNL concentrated on the design, fabrication and testing of SXR and tender x-ray (TXR) wavefront sensors designed for use on the next generation of diffraction-limited synchrotron beamlines. These are wavefront sensors intended for ultimate use as active feedback for mirror alignment and for adaptive x-ray optics that will be called upon to correct time-varying thermal and mechanical distortions occurring upstream. We believe that we can promote their adoption and greater use on beamlines worldwide if they can be made and operated in a relatively simple manner, using standard, inexpensive components where possible.

The key challenges in this area, different from most previous applications, are the narrow beam size at the detection location (0.5–2.5 mm), and a broad operating energy range, which may span an order of magnitude. A further complication comes from the desire to place the wavefront sensor upstream of the monochromator's exit slit where the energy bandwidth can be approximately 1% to 2%, and the light may be dispersed in one direction (from a grating monochromator). Consideration of potential non-invasive or intermittently invasive geometries led us to an off-axis design, that is adaptable to both types of applications. Furthermore, we wanted our systems to have few, and non-critical moving parts, to simplify operation and reduce cost.

Among the most significant innovations for the prototype wavefront sensors arose from the recognition that as feedback elements for a 1D adaptive mirror, rapid wavefront feedback may only be required in one direction. Thus, we created compact grating designs that allow us to fit numerous 1D gratings into the beam, with each grating tuned to a different operating energy. The configuration is described below.

6.1 Soft x-ray shearing and Hartmann wavefront sensor design at LBNL

Meeting the challenges led us through an investigation of the fundamental design constraints for single-grating shearing (a.k.a. Talbot) and Hartmann wavefront sensors, which have emerged as complementary yet interrelated methods that provide separate benefits. Shearing requires coherent light, while Hartmann does not rely on coherence. Shearing operates best close to diffraction-limited performance, while Hartmann can tolerate relatively large wavefront errors.

In a previous study [3], we observed that the Talbot distance $z = d^2/\lambda$, represents a fundamental length-scale for both shearing and Hartmann. (d is the pitch of the shearing grating or spacing of the Hartmann grid.) In shearing, the grating-to-detector separation is set to this self-imaging distance to produce high fringe contrast. (Note that other "fractional" and multiple distances are also used in certain instances, including the use of a phase-shifting grating, as mentioned previously.)

In the Hartmann configuration, diffraction promotes sensitivity, but the adjacent beamlets cannot overlap. With the grid holes occurring at a fraction of the hole pitch ($\sim 1/8$ is typical), we find that the optimal grid-to-detector spacing is a fraction of the shearing distance under comparable conditions. This led to a requirement of having two separate distances for the shearing grating and Hartmann grid, respectively, and a fixed detector plane. We note that the Hartmann grid-to-detector distance can be increased to match the shearing case, but this results in fewer grid periods within the beam width. Such tradeoffs must be evaluated for each application.

With mm-scale small (and converging) beam widths, and the need to operate off-axis, selecting an in-vacuum, direct-detection x-ray camera is not possible at this time for several reasons. The typical pixel sizes (above $5\ \mu\text{m}$) are prohibitively large for the required spatial sampling. Furthermore, an on-axis camera could block the straight-through beam path and putting significant constraints on the space around or alongside the detector.

We chose instead to use a yttrium aluminum garnet YAG(Ce) scintillator in conjunction with a visible-light microscope. The YAG is mounted to a right-angle prism to convert the interferogram or Hartmann-gram to visible-light and then reflect the light upward through a window into an at-air visible-light CCD camera, using a high-quality, $5\times$ microscope objective. In a compact arrangement, shown schematically in Fig. 17, the prism is glued directly to a vacuum window to minimize reflections and optical losses. The front-face of the prism is only 5 mm wide, so it is possible to have an unobstructed beam path passing just below it (in a non-invasive configuration), or for the prism/YAG to be moved up and down out of the beam (in an intermittently invasive configuration).

Minimizing the number of moving parts and simplifying our design made the prototype relatively inexpensive to create. Using standard optical elements and a visible-light lens and CCD outside of vacuum, further reduced the cost.



Figure 17. LEFT, Schematic LBNL wavefront sensor for SXR and TXR energies. CENTER, A shearing interferogram showing simultaneous illumination of many 1D gratings. The second grating from right satisfies the Talbot condition, and as the wavelength is tuned, the other gratings can be used. RIGHT, Hartmann-gram showing 2D wavefront measurement.

6.2 Wavefront sensor grating and grid designs optimized for 1D operation

The recognition that feedback for 1D adaptive mirror actuation comes most efficiently from 1D wavefront sensing led to the design decision to place numerous 1D gratings side by side. As the operating photon energy varies, the gratings, having different pitch values (d), satisfy the Talbot condition one at a time. We discovered that a single grating can be used without loss of accuracy across several percent energy change, and can thus operate in 1% or 2% bandwidth light. As we envision operation, the 1D wavefront sensing is in the direction orthogonal to the monochromator dispersion, so the 1D wavefront information is preserved (and not smeared). Two-dimensional (2D) wavefront sensing, from the shearing and Hartmann techniques is also available with this wavefront sensor when placed in a non-dispersed beam. We note that 1D measurement in this manner greatly increases the slope-measurement precision because it enables integration within the interferogram signal, in the direction parallel to the lines.

6.3 Creation of the transmission grating structures

With feature sizes ranging from 18 to $50\ \mu\text{m}$, we were able to use contact lithography and electroplating to create the grating structures on a transmission membrane, thus avoiding the complexity and uncertainty of large-area e-beam lithography, which is frequently required on related projects. Lithography was performed by LBNL's Center for X-Ray Optics (CXRO). Each "chip" contains four windows and numerous patterns that we can select among. One grating-array chip is shown in Fig. 18 with a schematic description of the design.

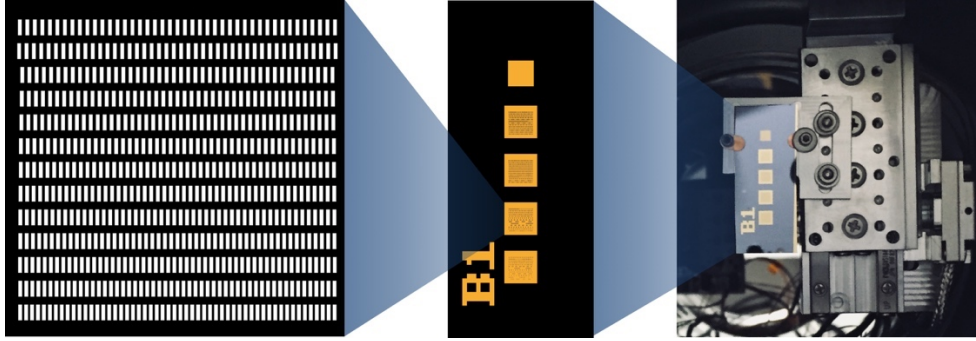


Figure 18. RIGHT, a vertical-translation stage holds the grating array created in five silicon-nitride membranes with a patterned gold absorber layer on a silicon wafer. The larger windows are 1.5 mm wide. The top window is for unobstructed transmission. Representations of the grating arrays, arranged for horizontal-direction shearing, are shown at RIGHT.

6.4 Wavefront sensor prototype testing at LBNL

A prototype constructed at LBNL was tested in Summer 2018, using SXR light from ALS Beamline 6.3.2, and in April 2019 with TXR light on ALS Beamline 5.3.1. The SXR results are described in Ref. 3, and representative data is shown in Fig. 19.

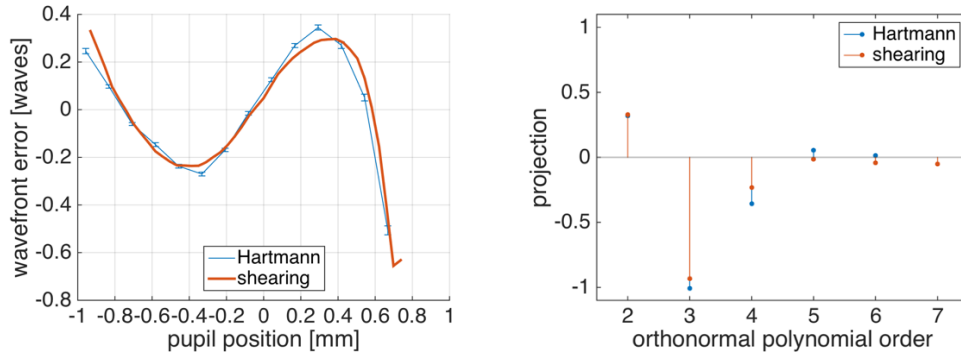


Figure 19. Comparison between the wavefront reconstruction from the shearing interferometer and the Hartmann wavefront sensors. (LEFT) Variation of the aberration at LH (with defocus term removed); the rms difference between the two measurements is $\lambda/78$ (32 pm). (RIGHT) Coefficients of an orthonormal polynomial basis describing the measured 1D wavefront.

For the SXR experiments, analysis showed that the separate shearing and Hartmann 1D wavefront measurements reached agreement on the wavefront shape to within $\lambda/35$ rms despite the fact that the measurements were independent, they use different physical principles, and they were analyzed in different ways.

Experiments at TXR energies (conducted in the approximate range of 3.5–4.0 keV) yielded important information about the required opacity of the Hartmann grid, and showed the impact of low coherence on the shearing measurements. In this case, the gold absorber thickness was suitable for Hartmann testing at SXR energies, but had insufficient opacity for TXR beams, leading to a strong *print-through* of the beam and degrading the measurement. For shearing, owing to low coherence on the bend-magnet beamline source, the fringe contrast never exceeded 5%.

7. SOFTWARE DEVELOPMENT

Several complementary software development efforts took place within this project, as described here.

7.1 Full-beamline simulations including Hartmann wavefront sensors in SRW

In simulation, we studied the alignment of Kirkpatrick-Baez (KB) optics [22, 23] with the goal of realizing a closed-loop alignment system using an at-wavelength wavefront sensor. The studies modeled a Hartmann Wavefront Sensor (HWS) used to detect aberrations in an x-ray optical system in a closed-loop alignment process, developed at BNL. The

Synchrotron Radiation Workshop (SRW) simulation code [24, 25] was used for these tests. Our goal was to design a new method to quickly decrease aberrations within a complex optical alignment, to perform ‘in situ’ KB mirror alignment, minimizing aberrations to reach a diffraction limited spot size. Before this implementation, no simulation packages or software had the ability to simulate the entire beamline, including the wavefront sensors. This model is available to be exported to other platforms through open collaboration agreements [26].

7.2 WAVEPY: An open source Python package for x-ray grating interferometry based wavefront sensors

Suitable, accessible data analysis software for grating-based interferometry (i.e. shearing/Talbot) is lacking within the x-ray optics community. To this end, we developed a Python-based open-source code called *WAVEPY*, tailored for data analysis of x-ray wavefront sensors. The software sets a framework for further development, aided by worldwide dissemination and collaboration. *WAVEPY* takes advantage of Python’s language capabilities and flexibility. It is designed to be expandable to facilitate collaboration, distribution, deployment, and integration with other wavefront sensors and imaging packages. The code is hosted on a Github repository [See Ref. 27]. It was used to process all of the APS-based wavefront measurements performed during this project.

7.3 ALS Wavefront tool for OASYS.

Ray-tracing tools such as SHADOW [28, 29] are commonly used in beamline design, and where coherent light propagation becomes important, ray tracing and wave propagation play complementary roles. Within the project we developed a new widget tool for the OASYS beamline modeling system [30, 31], to extract and analyze optical wavefronts based on the optical path lengths of rays. The open-source tool is called the ALS Wavefront Generator [31]. The wavefront description helps facilitate greater understanding of misalignments, thermal and mechanical deformations, and mirror surface errors in beamline modeling and simulations. It can also be used to test and optimize adaptive optics shapes to compensate wavefront aberrations. The new tool has been used to validate simulation results using experimental data based on wavefront sensor measurements, described in Section 4.4 and it is being used to develop and refine mirror surface, stability, and alignment tolerance specifications on new beamlines.

8. CONCLUSIONS

The four-lab collaboration described here sought to develop mirror and metrology technologies for the realization of optimal photon transport in beamline optical systems with diffraction-limited quality. Working collaboratively, the teams from ANL, BNL, LBNL, and SLAC, demonstrated wavefront correction using the REAL mirror adaptive-cooling system, and optimized a beamline alignment, in both cases applying in-situ wavefront sensing techniques.

The REAL mirror system is intended for use in high-incident-power conditions. The application of spatially distributed heating aims to create a uniform power load across a relevant length of the mirror, to inhibit thermal deformation. With the REAL mirror system, shape corrections were made by applying spatially varying power loads. Two methods of thermal contact were tested. We found that cooling through a series of Cu pads immersed in a trough filled with gallium-indium (GaIn) eutectic was superior to direct contact with indium foil pads. The gallium-indium approach provided greater control of the spatial distribution of the heating along the mirror’s surface, allowing improved shape correction relative to the indium foil approach. The REAL mirror system was engineered to operate in UHV conditions by adhering to strict control of the materials used in its fabrication.

The REAL mirror design was proven to work well for limited absorbed power. For high power wigglers or undulators, delivering several hundred watts, and for systems with power loads that vary on sub-minute timescales, we believe that the efficacy of this method may be limited. In fact, to compensate for large amount of absorbed power, it would be necessary to systematically increase the temperature of the mirror by several degrees, introducing other kinds of deformation. Rapidly changing conditions are difficult to achieve with REAL, because the thermal response time is on the order of several minutes. For higher power sources, cryogenically-cooled Si mirrors may be required to achieve diffraction-limited performance, provided that thermomechanical issues and the risks of carbon contamination can be mitigated.

Adaptive mirror tests, including wavefront optimizations, were performed at-wavelength using hard x-rays at APS beamline 7-ID. Shearing (Talbot) wavefront sensors were configured for both direct and non-invasive measurements using a diamond-film beam-splitter on a rotating arm. The viability of this approach was demonstrated by the achievement of rms wavefront errors as small as 15 pm (approximately $\lambda/5$) at 80-pm wavelength, after correction. The REAL mirror was tested in this way under varying power loads. A 19-channel piezo-bimorph adaptive mirror was similarly tested and achieved measured rms wavefront error values of 0.02λ and 0.11λ respectively in the diffracted and direct beams of the

non-invasive wavefront sensor. The method does have some limitations. For monochromatic beam sensing, the diamond beam splitter has to be oriented in the same diffraction direction as the monochromator. For white beam sensing, the crystal diffraction plane has to be perpendicular to the mirror reflection plane. The cooling of the thin crystal is another significant challenge for high power applications. Test at the APS showed that the pink beam after the mirror reflection has enough power to distort the thin crystal, preventing the linear response of the diffracted beam wavefront.

Wavefront sensors suitable for application on diffraction-limited SXR and HXR beamlines were developed and implemented to measure and characterize wavefronts. A commercial Hartmann wavefront sensor was used to optimize the alignment of the final focusing mirror on an ALS beamline. In addition, prototype tests were made of a new, combined shearing and Hartmann wavefront sensor system intended to serve as feedback for an adaptive mirror on diffraction-limited beamline optical system. The new design for SXR and TXR applications features a dense array of 1D shearing gratings (or Hartmann grids) that provide improved signal-to-noise for 1D measurements, and enable the wavefront sensor to span a wide operating energy range in a static configuration. To save cost, the system, including a YAG scintillator and a 5× visible-light microscope, was developed from commercially available components, and the grating was produced using contact lithography with feature sizes above 5 μm. Tests of the new design were conducted on SXR and TXR beamlines at the ALS.

Wavefront feedback will be mandatory for future high-coherent-flux beamlines and can be applied in many ways: for example, monitoring and optimizing the alignment of upstream beamline optics, as feedback to adaptively-shaped mirrors, compensating drifts and low-frequency vibration, and directly, where the interpretation of experimental data depends on understanding the wavefront shape with high accuracy. Developing robust and accurate feedback systems should be a high priority for groups worldwide developing state of the art beamline optical systems.

9. ACKNOWLEDGEMENTS

With the support of the Accelerator and Detector Research Program, part of the Scientific User Facility Division of the Basic Energy Science Office of the U.S. Department of Energy, under the Field Work Proposal numbers FWP# 100318, FWP# GoldbergWPM, FWP# 50513 and FWP#PS011

This work is performed under the auspices of the U.S. Department of Energy by LBNL under contract No. DE-AC02-05CH11231, SLAC under contract No. DE-AC02-76SF00515, ANL under contract No. DE-AC02-06CH11357 and BNL under contract No. DE-AC02-98CH10886.

We are gratefully acknowledged the facilities' leadership and management for their unwavering support to this project. Special thanks is due to the APS 7-ID beamline staff, particularly Don Walko, for their invaluable support throughout the experiment, and to Howard Padmore for his role in helping to form and support this collaborative effort. We appreciate Guillaume Dovillaire and the team from *Imagine Optics* for their development and support of Hartmann wavefront sensors.

REFERENCES

- [1] Zhang, L., Cocco, D., Kelez, N., Morton, D., Srinivasan, V., Stefan, P., "Optimizing X-ray mirror thermal performance using matched profile cooling," *J. Synchrotron Rad.* **22**, 1170–81 (2015).
- [2] Hardin, C. L., Srinivasan, V. N., Amores, L., Kelez, N. M., Morton, D. S., Stefan, P. M., Nicolas, J., Zhang, L., and Cocco, D., "Optimizing x-ray mirror thermal performance using variable length cooling for second generation FELs," *Proc. SPIE* **9965**, 996505 (2016).
- [3] Wojdyla, A., Bryant, D., Goldberg, K. A., Assoufid, L., Cocco, D., Idir, M., "Design and Demonstration of tunable lateral shearing and Hartmann soft x-ray wavefront sensors," *Proc. SPIE* **10760**, 1076003 (2018).
- [4] Marathe, S., Shi, X., Khounsary, A. M., Wojcik, M., J., Kujala, N. G., Macrander, A. T., Assoufid, L., "Development of single grating x-ray Talbot interferometer as a feedback loop sensor element of an adaptive x-ray mirror system," *Proc. SPIE* **9208**, 92080D (2014).
- [5] Grizolli, W., Shi, X., Kolodziej, T., Shvyd'ko, Y., Assoufid, L., "Single-grating Talbot imaging for wavefront sensing and x-ray metrology," *Proc. SPIE* **10385**, 1038502 (2017).
- [6] Kearney, S. P., Assoufid, L., Grizolli, W., Kolodziej, T., Lang, K., Macrander, A., "Mechanical design of a compact non-invasive wavefront sensor for hard X-ray," *Proc. MEDSI 2018 Conference* (pp. 394–396).

- [7] Assoufid, L. *et al.* “Development of a hard X-ray non-invasive wavefront sensor using a single-grating interferometer combined with a thin diamond single-crystal beam splitter,” *2018 International Conference on X-ray Optics and Application (XOT)*, Yokohama, Japan, April 24, 2018.
- [8] Naulleau, P. P., Goldberg, K. A., and Bokor, J., “Extreme ultraviolet carrier-frequency shearing Interferometry of a lithographic four-mirror optical system,” *J. of Vac. Sci. & Technol. B* **18** (6), 2939–43 (2000).
- [9] Merthe, D. J., Goldberg, K. A., Yashchuk, V. V., McKinney, W. R., Celestre, R., Mochi, I., MacDougall, J., Morrison, G. Y., Rekawa, S. B., Anderson, E., Smith, B. V., Domning, E. E., Padmore, H., “In situ fine tuning of bendable soft x-ray mirrors using a lateral shearing interferometer,” *Nucl. Instr. Meth. Phys. Res. A* **710**, 82 (2013).
- [10] Malacara, D., [Optical Shop Testing], Wiley-Interscience; 2nd edition, Ch. 10 (1992).
- [11] Mercère, P., Zeitoun, P., Idir, M., Le Pape, S., Douillet, D., Levecq, X., Dovillaire, G., Bucourt, S., Goldberg, K. A., Naulleau, P. P., and Rekawa, S., “Hartmann wave-front measurement at 13.4 nm with $\lambda_{\text{EUV}}/120$ accuracy,” *Opt. Lett.* **28** (17), 1534–36 (2003).
- [12] Mercère, P., Idir, M., Moreno, T., Cauchon, G., Dovillaire, G., Levecq, X., Couvet, L., Bucourt, S., and Zeitoun, P., “Automatic alignment of a Kirkpatrick–Baez active optic by use of a soft-x-ray Hartmann wavefront sensor,” *Opt. Lett.* **31** (2), 199–201 (2006).
- [13] Mochi, I., Goldberg, K. A., “Modal wavefront reconstruction from its gradient,” *Appl. Opt.* **54** (12), 3780–85 (2015).
- [14] Huang, L., Idir, M., Zuo, C., Kaznatcheev, K., Zhou, L., Asundi, A., “Shape reconstruction from gradient data in an arbitrarily-shaped aperture by iterative discrete cosine transforms in Southwell configuration,” *Opt. Lasers Eng.* **67**, 176–81 (2015).
- [15] Huang, L., Xue, J., Gao, B., Zuo, C., Idir, M., “Spline based least squares integration for two-dimensional shape or wavefront reconstruction,” *Opt. Lasers Eng.* **91**, 221–26 (2017).
- [16] Huang, L., Xue, J., Gao, B., Zuo, C., Idir, M., “Zonal wavefront reconstruction in quadrilateral geometry for phase measuring deflectometry,” *Appl. Opt.*, **56** (18), 5139–44 (2017).
- [17] Huang, L., Idir, M., Zuo, C., Kaznatcheev, K., Zhou, L., Asundi, A., “Comparison of two-dimensional integration methods for shape reconstruction from gradient data,” *Opt. Lasers Eng.*, **64**, 1–11 (2015).
- [18] Wojdyla, A., Bryant, D., Goldberg, K. A., Assoufid, L., Cocco, D., Idir, M., “Design of shearing and Hartmann wavefront sensors for diffraction-limited beamlines,” presented at the International Workshop on X-Ray Metrology (IWXM), Hsinchu, Taiwan, June 15, 2018.
- [19] Marathe, S., Shi, X., Wojcik, M. J., Kujala, N. G., Divan, R., Mancini, D. C., Macrander, A. T., Assoufid, L., “Probing transverse coherence of x-ray beam with 2-D phase grating interferometer,” *Opt. Express* **22** (12), 14041–53 (2014).
- [20] Assoufid, L., Shi, X., Marathe, S., Benda, E., & Wojcik, M. J., “Development and implementation of a portable grating interferometer system as a standard tool for testing optics at the Advanced Photon Source beamline 1-BM,” *Rev. Sci. Instrumen.* **87** (5), 052004 (2016).
- [21] JTEC Corp., Japan, <http://www.j-tec.co.jp>.
- [22] Kirkpatrick, P., and Baez, A. V., “Formation of Optical Images by X-Rays,” *J. Opt. Soc. Am.*, **38** (9), 766–74 (1948).
- [23] Suzuki, Y., Uchida, F., “X-Ray Focusing with Elliptical Kirkpatrick-Baez Mirror System,” *Jpn. J. Appl. Phys.*, **30** (5), 1127–30 (1991).
- [24] Chubar, O., Fluerasu, A., Berman, L., Kaznatcheev, K., Wiegart, L., “Wavefront propagation simulations for beamlines and experiments with “Synchrotron Radiation Workshop,” *J. Phys.: Conf. Ser.* **425** 162001 (2013).
- [25] Idir, M., Rakitin, M., Gao, B., Xue, J., Huang, L., Chubar, O., “Alignment of KB mirrors with at-wavelength metrology tool simulated using SRW,” *Proc. SPIE* **10388**, 103880Z (2017).
- [26] SRW on Github, <https://github.com/ochubar/SRW>.
- [27] The WAVEPY Python Library, <https://github.com/wavepy/wavepy>.
- [28] Lai, B., Cerrina, F. “SHADOW: A synchrotron radiation ray tracing program,” *Nucl. Instr. Meth. Phys. Res. A* **246**, 337–41 (1986).
- [29] Sanchez del Rio, M., Canestrari, N., Jiang, F., and Cerrina, F., “SHADOW3: a new version of the synchrotron X-ray optics modelling package,” *J. Synchrotron Rad.* **18**, 708–16 (2011).
- [30] Rebuffi, L., Sanchez del Rio, M., “ShadowOui: A new visual environment for X-ray optics and synchrotron beamline simulations,” *J. Synchrotron Rad.*, **23**, 1357–67 (2016).
- [31] Rebuffi, L., Sanchez del Rio, M., “OASYS (OrAnge SYNchrotron Suite): an open-source graphical environment for x-ray virtual experiments,” *Proc. SPIE* 10388, 103880S (2017).
- [32] Wojdyla, A., GitHub: <http://github.com/oasys-als-kit/OASYS1-ALS-ShadowOui.git>